

MATERIAL SCIENCE

Nanoscale strain engineering of giant pseudo-magnetic fields, valley polarization, and topological channels in graphene

C.-C. Hsu^{1*}, M. L. Teague^{1*}, J.-Q. Wang^{1*}, N.-C. Yeh^{1,2†}

The existence of nontrivial Berry phases associated with two inequivalent valleys in graphene provides interesting opportunities for investigating the valley-projected topological states. Examples of such studies include observation of anomalous quantum Hall effect in monolayer graphene, demonstration of topological zero modes in “molecular graphene” assembled by scanning tunneling microscopy, and detection of topological valley transport either in graphene superlattices or at bilayer graphene domain walls. However, all aforementioned experiments involved nonscalable approaches of either mechanically exfoliated flakes or atom-by-atom constructions. Here, we report an approach to manipulating the topological states in monolayer graphene via nanoscale strain engineering at room temperature. By placing strain-free monolayer graphene on architected nanostructures to induce global inversion symmetry breaking, we demonstrate the development of giant pseudo-magnetic fields (up to ~ 800 T), valley polarization, and periodic one-dimensional topological channels for protected propagation of chiral modes in strained graphene, thus paving a pathway toward scalable graphene-based valleytronics.

INTRODUCTION

It has been well recognized that the Berry curvature of electronic wave functions can have a profound effect on the physical properties of materials (1–3). For instance, nontrivial Berry curvatures in the event of either broken time-reversal symmetry or broken inversion symmetry are known to be responsible for various (quantum, anomalous, spin, and valley) Hall effects (3–6). In the case of graphene with gapless Dirac cones at the two inequivalent valleys K and K', the spinor-type wave functions of the Dirac fermions result in nontrivial Berry phases of π and $-\pi$ (7–9). For perfect and flat monolayer graphene in the absence of an external magnetic field, the Berry flux from K and K' exactly cancels each other so that the Hall conductance vanishes under both time and inversion symmetries (7–9). On the other hand, inversion symmetry can be broken by either atomically aligning monolayer graphene on top of hexagonal boron nitride (h-BN) (10) or artificially building in the broken inversion symmetry in strained “molecular graphene” assembled by scanning tunneling microscopy (STM) (11). The former leads to the realization of the valley Hall effect (VHE) (10), and the latter manifests Landau quantization and site-dependent topological zero modes in the tunneling conductance spectra (11). In addition, one-dimensional (1D) valley-polarized conducting channels associated with the protected chiral edge states of quantum valley Hall insulators have been demonstrated at the domain walls between AB- and BA-stacked bilayer graphene (12). These interesting results underscore the rich opportunities provided by graphene-based systems for the studies of valley-projected topological states.

In contrast, while monolayer transition-metal dichalcogenides (TMDCs) in the 2H-phase are 2D semiconducting crystals with an in-plane structure similar to graphene and exhibit strong spin-valley coupling and interesting optical properties (13–16), no discernible

out-of-the-plane pseudo-magnetic fields can be induced by strain due to negligible Berry curvatures around the gapped bands at the K and K' points (17). Thus, the primary strain-induced effect on 2D TMDCs is only associated with the modification to the semiconducting energy gaps, leading to brighter photoluminescence in stronger strained areas due to the resulting smaller energy gaps (17, 18).

Earlier experimental investigations of strained graphene generally involve approaches of either stacking mechanically exfoliated, microscale flakes of graphene on h-BN (10) or assembling atom by atom using a scanning tunneling microscope (11). Neither method is scalable for realistic device applications. Recently, efforts have been made to pre-design the substrate to induce controlled strain on monolayer graphene (19–24). However, most of these strained graphene samples have only been characterized by imaging with scanning electron microscopy (SEM) and/or atomic force microscopy (AFM) and by Raman spectroscopy without explicit investigation of the strain-induced pseudo-magnetic field (19–23). In the only case of direct measurements of the pseudo-magnetic fields by means of STM/scanning tunneling spectroscopy (STS), studies were solely carried out in nearly flat areas with much smoother topography so that the resulting pseudo-magnetic fields were very small (~ 7 T) and were taken at low temperatures (~ 4.6 K) (24). Here, we report a scalable experimental approach that successfully induces giant pseudo-magnetic fields (up to ~ 800 T) and achieves manipulation of the topological states and in monolayer graphene by means of nanoscale strain engineering at room temperature. Our methodology involves placing a nearly strain-free, large-area (~ 1 cm²) monolayer graphene sheet on top of properly architected nanostructures to induce global inversion symmetry breaking. We demonstrate the development of strain-induced giant pseudo-magnetic fields and global valley polarization by direct STM/STS studies. The experimental investigations are further corroborated by simulations using the molecular dynamics (MD) method elaborated in the Supplementary Materials and figs. S1 to S3. We also verify the feasibility of periodic 1D topological channels for protected propagation of chiral modes in graphene based on our empirically demonstrated periodic strain patterns and MD simulations. This methodology is shown to be scalable and

Copyright © 2020
The Authors, some
rights reserved;
exclusive licensee
American Association
for the Advancement
of Science. No claim to
original U.S. Government
Works. Distributed
under a Creative
Commons Attribution
NonCommercial
License 4.0 (CC BY-NC).

¹Department of Physics, California Institute of Technology, Pasadena, CA 91125, USA. ²Kavli Nanoscience Institute, California Institute of Technology, Pasadena, CA 91125, USA.

*These authors contributed equally to this work.

†Corresponding author. Email: ncyeh@caltech.edu

controllable, which paves a new pathway toward realizing realistic graphene-based valleytronic applications.

RESULTS

Nanoscale strain engineering of graphene

Our experimental approach is based on the notion that the electronic properties of graphene exhibit significant dependence on the nanoscale structural distortion and the resulting strain (7, 25–31). In general, structural distortion-induced strain in the graphene lattice gives rise to two primary effects on the Dirac fermions (13, 15). One is an effective scalar potential Φ , and the other is an effective gauge potential \mathbf{A} related to the Berry connection in the reciprocal space (25, 27). These strain-induced effective scalar and gauge potentials in graphene are the consequences of the changes in the distance or angle between the p_z orbitals due to structural distortions, which modify the hopping energies between Dirac electrons at different lattice sites, thereby giving rise to the addition of an effective gauge potential \mathbf{A} and a scalar potential Φ to the original Dirac Hamiltonian of ideal monolayer graphene. The excess scalar potential can cause scattering of Dirac fermions and changes in the local charge densities, whereas the excess gauge potential can result in a pseudo-magnetic field that is related to the Berry curvatures in the reciprocal space and couples with the valley (pseudo-spin) degrees of freedom. Thus, proper nanoscale engineering of the strain in graphene can provide unique means to manipulate the valley degrees of freedom (29). Moreover, by combining large-scale strain-free graphene and modern nanofabrication technology, it becomes feasible to devise scalable structures to achieve desirable control of the valley-associated topological states.

To achieve large-area ($\sim 1 \text{ cm}^2$) nearly strain-free graphene, we used the plasma-enhanced chemical vapor deposition (PECVD) technique, as detailed previously (32). To induce controlled nanoscale strain on initially strain-free graphene, we carried out the procedures schematically illustrated in Fig. 1A. Specifically, two different approaches were taken to induce substantial strain. The first approach involved fabricating Pd nanocrystals (NCs) that were in the form of tetrahedrons with a typical base of $\sim 30 \text{ nm}$ in length, using a wet chemical method first developed by Zhang *et al.* (33) and further

elaborated in Materials and Methods. The second approach involved fabricating periodic arrays of nanostructures on silicon substrates using either electron beam (e-beam) lithography or focused ion beam (FIB) lithography, as detailed in Materials and Methods and further illustrated in fig. S4. The NCs were dispersed on a silicon substrate, as exemplified by the SEM images over an area of $3 \mu\text{m} \times 3 \mu\text{m}$ shown in Fig. 1B and for a zoom-in view of two NCs shown in Fig. 1C. Next, we transferred a monolayer of h-BN and then a monolayer of our PECVD-grown monolayer graphene on top of the NCs by means of a polymer-free technique (34), where the h-BN was mechanically exfoliated either from an h-BN single crystal or by the CVD growth method developed by Lin *et al.* (35). Both the h-BN and graphene monolayers were shown to conform well to separated NCs, as illustrated in Fig. 1D and the upper panel in Fig. 1E. However, for closely spaced NCs, a wrinkle in graphene appeared, as exemplified in the lower panel of Fig. 1E. Here, we note that the purpose of inserting an h-BN monolayer between graphene and silicon nanostructures is to minimize the effects of phonon coupling between Si and graphene (28) and of charge impurities in the Si substrate (28) on graphene.

The structural distortion-induced strain on graphene can be evaluated using the strain tensors. For a spatially varying displacement field $\mathbf{u} \equiv u_x \hat{x} + u_y \hat{y} + h \hat{z}$, the strain tensor components u_{xx} , u_{xy} , and u_{yy} are given by (25, 27)

$$\begin{aligned} u_{xx} &= \frac{\partial u_x}{\partial x} + \frac{1}{2} \left(\frac{\partial h}{\partial x} \right)^2, \quad u_{xy} = \frac{1}{2} \left(\frac{\partial u_x}{\partial y} + \frac{\partial u_y}{\partial x} \right) + \frac{1}{2} \left(\frac{\partial h}{\partial x} \frac{\partial h}{\partial y} \right), \\ u_{yy} &= \frac{\partial u_y}{\partial y} + \frac{1}{2} \left(\frac{\partial h}{\partial y} \right)^2 \end{aligned} \quad (1)$$

If the x axis is chosen along the zigzag direction, the 2D strain-induced gauge potential in the real-space $\mathcal{A} = A_x \hat{x} + A_y \hat{y}$ can be expressed in terms of the tensor components by the following relations (in the first-order approximation) (7)

$$A_x = \pm \frac{\beta}{a_0} (u_{xx} - u_{yy}), \quad A_y = \mp 2 \frac{\beta}{a_0} u_{xy} \quad (2)$$

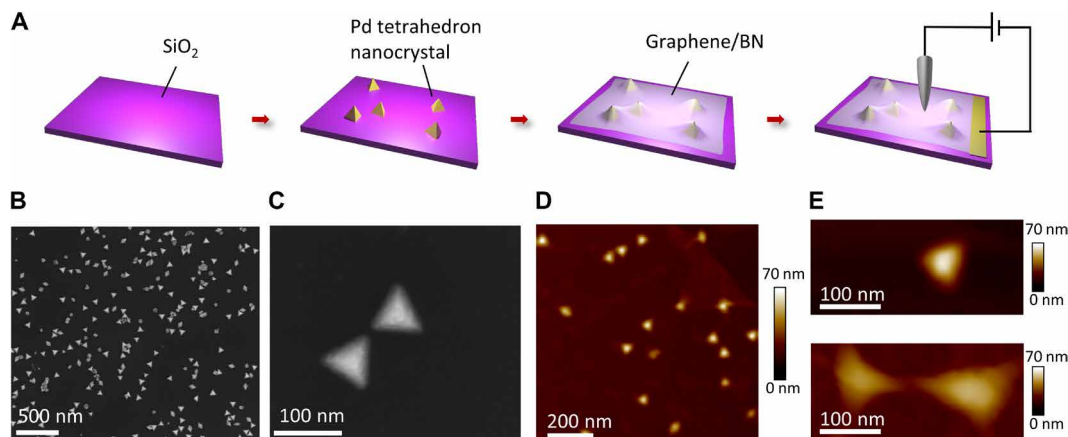


Fig. 1. Nanoscale strain engineering of graphene. (A) Schematic illustrations showing the steps taken to induce strain on graphene by Pd tetrahedron NCs. (B) SEM image of randomly distributed Pd tetrahedron NCs distributed on a Si substrate over an area of $3 \mu\text{m} \times 3 \mu\text{m}$. (C) A zoom-in SEM image of two Pd tetrahedron NCs. (D) Exemplifying AFM image of graphene/h-BN/Pd tetrahedron NCs. (E) Top: AFM image of graphene/h-BN on a single Pd tetrahedron NC, showing excellent conformation of graphene/h-BN to the single Pd tetrahedron NC. Bottom: AFM image of graphene/h-BN on two closely spaced Pd tetrahedron NCs, showing the formation of a graphene wrinkle between the two Pd tetrahedron NCs.

where $a_0 \approx 0.142$ nm is the nearest carbon-carbon distance for equilibrium graphene, β is a constant ranging from 2 to 3 in units of the flux quantum, and the upper and lower signs are associated with the K and K' valleys, respectively (7). From Eq. 1, we note that in the event of strong z -axis corrugation, the strain components resulting from the height variations becomes dominant over the in-plane strain components, as exemplified in figs. S1 to S3. Using Eqs. 1 and 2, the spatial distribution of the pseudo-magnetic field can be obtained according to $B_S(\mathbf{r}) = \nabla \times \mathbf{A}(\mathbf{r})$, with opposite signs associated with the K and K' valleys so that the global time reversal symmetry is preserved and the total flux integrated over the entire sample is zero. Hence, from given 3D atomic structural distortions of graphene, which may be determined by either STM or high-resolution AFM, the spatial variations of $B_S(\mathbf{r})$ can be derived.

Alternatively, the magnitude of pseudo-magnetic field, $|B_S(\mathbf{r})|$, can be independently verified by spatially resolved STS, where the pseudo-magnetic field-induced quantized Landau levels E_n (with n being integers) in the tunneling conductance (dI/dV) versus biased voltage ($V = E/e$, with E being quasi-particle energy) spectrum at a given position \mathbf{r} satisfy the following relation

$$E_n = \text{sgn}(n) \sqrt{2ev_F^2 \hbar |nB_S|}, \Rightarrow |B_S| = [(E_{n+1})^2 - (E_n)^2] / (2ev_F^2 \hbar) \quad (3)$$

Using Eq. 3, the magnitude of the pseudo-magnetic field at a given position can be determined rigorously by the energy spacing of different Landau levels of varying indices n in the local tunneling spectrum. The consistency of such spectroscopic studies with the value obtained from the strain tensors can be verified by comparing with the atomically resolved topographic studies.

Topographic and spectroscopic evidences for the formation of giant pseudo-magnetic fields

In Fig. 2, we illustrate the comparison of the strain-induced pseudo-magnetic fields for the K valley from both topographic and spectroscopic studies at room temperature. The main panels of Fig. 2 (A and B) are respectively zoom-out AFM and STM topographic images over an area of $100 \text{ nm} \times 100 \text{ nm}$ that cover the full view of monolayer graphene/h-BN over an isolated Pd tetrahedron. In the inset of Fig. 2A, a zoom-in atomically resolved STM topography of graphene over an area of $3 \text{ nm} \times 3 \text{ nm}$ near the tip of the tetrahedron reveals strong structural distortion in graphene with significant height displacements. Assuming the validity of first-order strain-induced perturbation to the Dirac Hamiltonian and using the MD method as detailed in the Supplementary Materials, we obtain the resulting pseudo-magnetic field distributions in Fig. 2C for the topography shown in Fig. 2B. In addition, maps of the corresponding strain tensors are provided in fig. S5 (A to C). Given the significant structural distortions in graphene, we note the resulting large magnitudes of the pseudo-magnetic field, up to ~ 800 T in maximum values if computed from the topographic information.

Concurrent spectroscopic studies of the strained graphene over the isolated tetrahedron also revealed spatially varying tunneling spectra, as exemplified in Fig. 2D for a collection of high-resolution tunneling conductance versus bias voltage spectra along the black line indicated in Fig. 2C. Here, the horizontal axis in Fig. 2D corresponds to the bias voltage, the vertical axis corresponds to the spatial dimension along the black line (from lower left to upper right) in Fig. 2C, and the colors represent the tunneling conductance difference from the unstrained graphene. The 3D representation of the tunneling spectra taken along the same line cut is shown in Fig. 2E. Specifically, a typical V-shaped tunneling spectrum for ideal graphene is shown

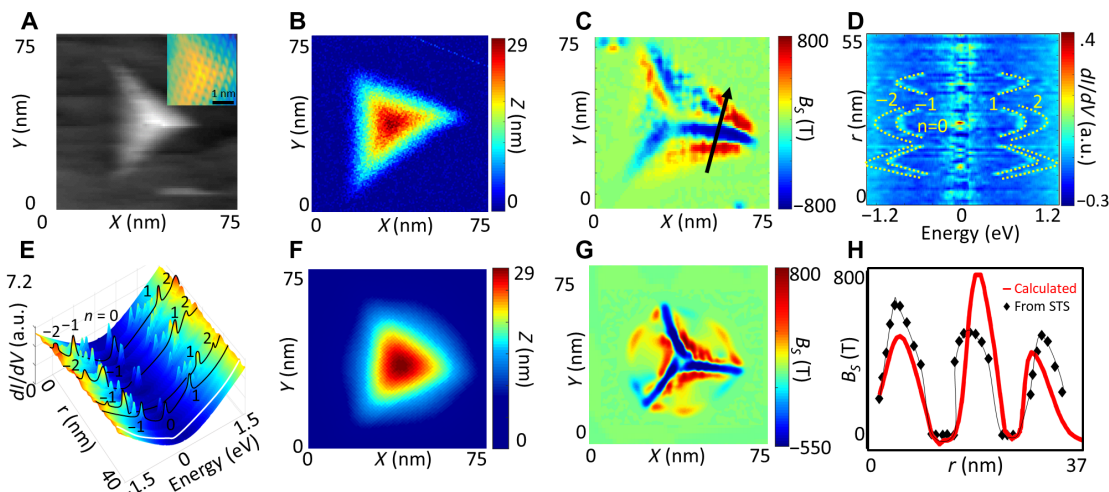


Fig. 2. Topographic and spectroscopic studies of strain-induced effects on graphene at room temperature due to one Pd tetrahedron NC. (A) 3D topographic images of the distorted graphene taken by AFM (main panel) and by STM (inset, zoom-in image with atomic resolution). (B) 3D topographic image of the distorted graphene taken by STM. (C) Pseudo-magnetic field map calculated from the topography over the same area as shown in (B). (D) Tunneling conductance spectral difference relative to the Dirac spectrum of strain-free graphene is shown along the line cut indicated by the black arrow in (C), revealing spatially varying strengths of strain-induced pseudo-magnetic fields as manifested by the variations in the Landau-level separation. a.u., arbitrary units. (E) Representative spectra of tunneling conductance versus energy of strained graphene along the black line cut in (C), showing quantized conductance peaks in strained regions and the V-shape Dirac spectrum in strain-free regions as exemplified by the white curve located at $r \sim 36$ nm. (F) 3D topographic map of graphene/h-BN deformation on an ideal tetrahedron, as computed from MD simulations described in the Supplementary Materials. (G) Pseudo-magnetic field map computed from the topographic distortion in (F). (H) Comparison of the absolute values of pseudo-magnetic fields $|B_S(r)|$ derived from topographic studies (red line) and from the Landau-level separations in STS (black diamonds), showing overall satisfactory agreement. Here, r denotes the distance measured from the lower-left end to the upper-left end of the black arrow shown in (C).

in the strain-free region, as exemplified by the white curve in Fig. 2E, whereas increasing larger energy separations for consecutive peak features are found for the tunneling spectra taken at increasingly strained regions, showing a consistent increase in the Landau-level energy separations with the increasing magnitude of strain found in the topographic studies.

To further verify the consistency between the magnitude of pseudo-magnetic field determined from topography and from spectroscopy, we compare in Fig. 2H the absolute values of pseudo-magnetic fields $|B_S(r)|$ derived from topographic studies (Fig. 2C) and those from the Landau-level separations (Fig. 2D) using Eq. 3 and find overall reasonable agreement. Here, r denotes the distance measured from the lower-left end to the upper-left end of the black arrow in Fig. 2C. In addition, we carried out MD simulations for the topography and pseudo-magnetic field map of monolayer graphene/h-BN strained by a perfect tetrahedron with a base dimension of 30 nm, as shown in Fig. 2 (F and G). These MD simulations are largely consistent with the experimental results shown in Fig. 2 (B and C), although it is difficult to achieve detailed agreement due to unknown microscopic interaction parameters between the monolayer graphene/h-BN and the underlying nano-tetrahedron that are required to carry out the MD simulations.

To better manifest the characteristics of point spectra taken on areas of strained graphene, we show, in fig. S6A, four point spectra taken on highly strained locations indicated as α , β , γ , and δ on the pseudo-magnetic field map in fig. S6B (which is the same pseudo-magnetic field map as in Fig. 2C), where the corresponding pseudo-magnetic fields are $|B_S(r)| \sim 600$ T and the resulting Landau levels $n = 0, \pm 1, \pm 2$, and ± 3 are explicitly indicated. In addition, a theoretical fitting curve for one of the point spectra with $|B_S(r)| = 592$ T is shown in fig. S6C, demonstrating that the superposition of Lorentzian Landau levels on top of a background Dirac spectrum achieves good agreement with the experimental data. We further note that for all point spectra taken in strained graphene areas, approximately half of the spectra reveal a zero-bias conductance peak that corresponds to a Landau level with $n = 0$, whereas the other half of the spectra are without a zero-bias Landau level. This phenomenon is

the result of two zero modes associated with spontaneous local time-reversal symmetry breaking, which will be investigated further in Discussion.

Next, we consider the strain on graphene induced by two closely spaced nano-tetrahedrons, as manifested by the topography in Fig. 3 (A and B) and the corresponding pseudo-magnetic field map for the K valley in Fig. 3C. In addition, maps of the strain tensors associated with Fig. 3B are given in fig. S7 (A to C). We found that the maximum magnitude for the pseudo-magnetic field computed from the structural distortion was ~ 600 T (Fig. 3C), smaller than that found in the case of single tetrahedron (Fig. 2C). This is because comparable height displacements to those in Fig. 2B were spread over a larger lateral dimension in the case of two closely spaced tetrahedrons so that the magnitude of $(\partial h/\partial i)$ ($\partial h/\partial j$) becomes significantly reduced, where i and j denote either x or y coordinate. Moreover, detailed comparisons of the spectroscopically determined pseudo-magnetic fields [as exemplified in Fig. 3D for the line cut spectra along the white dashed line and in Fig. 3 (E and H) for the line cut spectra along the black dashed lines in Fig. 3C] with those determined topographically (Fig. 3C) were found to be in good agreement quantitatively.

In addition to verifying the consistency between the topographic and spectroscopic derivations of strain-induced pseudo-magnetic fields, the development of a topographic “wrinkle” between two nearby nanostructures is noteworthy. Moreover, the resulting pseudo-magnetic fields along the wrinkle direction appeared to form quasi-1D “channels” of nearly uniform pseudo-magnetic fields, whereas those perpendicular to the wrinkle exhibited relatively rapid and continuous spatial variations with alternating signs. This formation of a topographic wrinkle in graphene between two nanostructures provides a hint for developing controlled and spatially extended strain to achieve global inversion symmetry breaking, which is the subject of our following exploration.

Formation of periodic parallel graphene wrinkles for valley splitting and as topological channels

Next, we used nanofabrication technology to develop regular arrays of nano-cones on silicon with processes described in Materials and

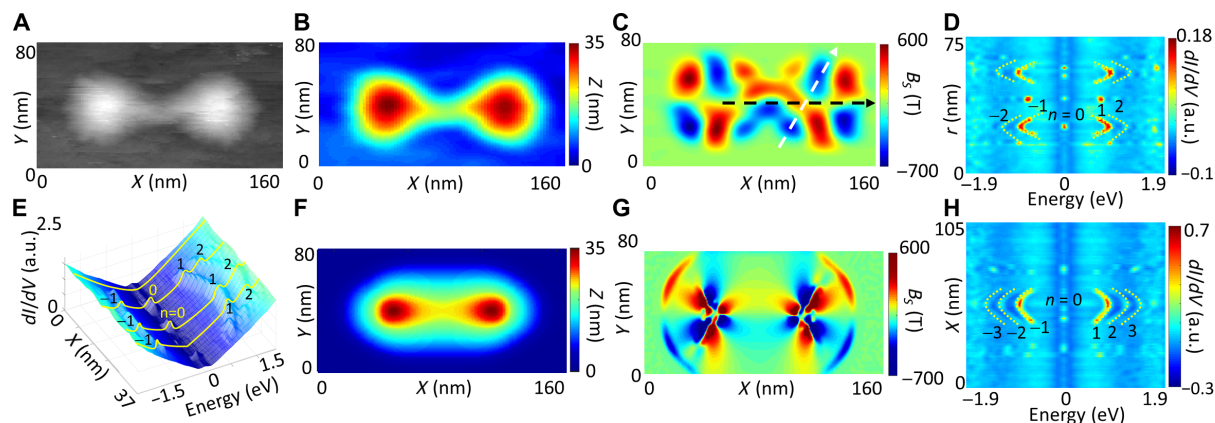


Fig. 3. Topographic and spectroscopic studies of strain-induced effects on graphene due to two closely separated Pd tetrahedron NCs. (A) 3D topographic image of the distorted graphene taken by AFM. (B) 3D topographic image of the distorted graphene taken by STM. (C) Pseudo-magnetic field map calculated from the topography over the same area as shown in (B). (D) Tunneling conductance spectral difference from the Dirac spectrum along the line cut shown by the white dashed line in (C). (E) Spatially resolved tunneling spectra of strained graphene along the black dashed line in (C), showing strain-induced quantized conductance peaks. (F) 3D topographic map of graphene/h-BN on two ideal tetrahedrons computed from MD simulations. (G) Pseudo-magnetic field map computed from topographic distortion shown in (F). (H) Tunneling conductance spectral difference relative to the Dirac spectrum along the line cut shown by the black dashed line in (C).

Methods and schematically illustrated in fig. S4. Two types of periodic arrays were explored. One was a triangular lattice structure and the other was a rectangular lattice structure, as shown by the SEM images in the top panels of Fig. 4, A and B, respectively. We found that the wrinkles induced on monolayer graphene by a triangular lattice had the tendency of forming along any of the three equivalent directions, as shown by the SEM image in the bottom panel of Fig. 4A. In contrast, wrinkles induced by the rectangular lattice were generally well aligned and parallel to each other, as exemplified by the SEM image in the bottom panel of Fig. 4B and the AFM images in the top panels of Fig. 4 (C and D). The corresponding pseudo-magnetic fields associated with the graphene distortions in the top panels of Fig. 4 (C and D) are computed from the topography and shown in bottom panels of Fig. 4 (C and D).

It is worth noting that each extended graphene wrinkle results in four parallel, relatively uniform pseudo-magnetic fields along one direction and varying with alternating signs perpendicular to the channels, as illustrated in the bottom panel of Fig. 4D. Given that the pseudo-magnetic fields as observed by K and K' Dirac fermions are opposite in sign, the formation of parallel channels of pseudo-magnetic fields can effectively result in valley splitting and valley polarization. As illustrated by the theoretical simulations in the upper panels of Fig. 5 (A and B) and further detailed in the Supplementary Materials, for valley-degenerate Dirac fermions incident perpendicular to the parallel channels of pseudo-magnetic fields, K- and K'-valley fermions can become spatially separated and the lateral separation will increase with the increasing number of wrinkles they pass over, provided that the average separation (d) of consecutive wrinkles is less than the ballistic length (l_B) of Dirac fermions.

Specifically, the ballistic length l_B is related to the conductance (G), mobility (μ), and carrier density (n_{2D}) of Dirac fermions in monolayer graphene by the following relation (7)

$$G = \frac{2e^2}{2\pi\hbar}(k_F l_B) = n_{2D} e \mu, \Rightarrow l_B = \left(\frac{2\pi\hbar}{2e} \right) \frac{n_{2D} \mu}{k_F} = \left(\frac{\hbar}{e} \right) \mu \sqrt{\pi n_{2D}} \quad (4)$$

where $k_F = (n_{2D}\pi)^{1/2}$ is the Fermi momentum, e is the electron charge, and $2\pi\hbar$ denotes the Planck constant. For typical values of $n_{2D} = 10^{10}$ to 10^{12} cm^{-2} and $\mu \sim 10^5 \text{ cm}^2/\text{V-s}$ for our PECVD-grown graphene, we find that $l_B = 120 \text{ nm}$ to $1.2 \mu\text{m}$. Thus, by proper nanofabrication to design the d value and by gating the PECVD-grown graphene for suitable n_{2D} and l_B , the condition $d < l_B$ can be satisfied within realistic experimental parameters to achieve valley splitting and therefore valley polarized currents.

In addition to yielding valley splitting as discussed above, the parallel distributions of alternating signs of pseudo-magnetic fields can serve as topological channels for chiral fermions. As shown in Fig. 5C, theoretical simulations for realistic arrays of nanostructures reveal that chiral Dirac fermions (i.e., either K or K' fermions) can be preserved when propagate along the parallel channels of strain-induced pseudo-magnetic fields, as illustrated by the simulations shown in the top panel of Fig. 5C. In addition, valley-polarized Dirac fermions can even be collimated along the topological channels if the incident angle deviates slightly from the channel direction, as exemplified in the bottom panel of Fig. 5C. Thus, parallel graphene wrinkles can serve as an effective conduit for protected propagation of valley-polarized Dirac fermions.

DISCUSSION

Spontaneous local time-reversal symmetry breaking and the resulting two zero modes

Although the strain-induced pseudo-magnetic fields do not break the global time-reversal symmetry, the gauge potentials A and A^*

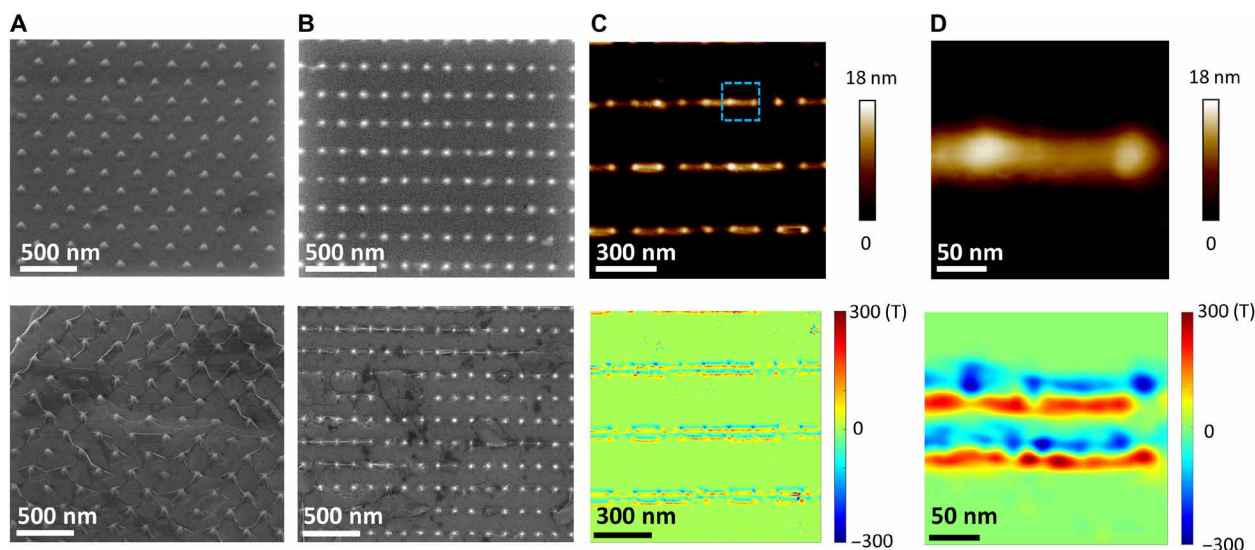


Fig. 4. Extended strain effects induced by periodic arrays of nano-cones on graphene. (A) Top: SEM image of triangular arrays of cone-shaped nanostructures fabricated on a SiO_2/Si substrate. Bottom: SEM image of monolayer-graphene/h-BN films on the triangular arrays shown in the top panel, showing graphene wrinkles that appeared randomly along three equivalent directions. (B) Top: SEM image of rectangular arrays of cone-shaped nanostructures fabricated on a SiO_2/Si substrate. Bottom: SEM image of monolayer-graphene/h-BN films on the rectangular arrays shown in the top panel, showing graphene wrinkles parallel to the axis of closer spaced nanostructures. (C) AFM image (top) of three parallel graphene wrinkles and the corresponding map of pseudo-magnetic fields derived from the strain tensors (bottom). (D) AFM image (top) of the graphene wrinkle enclosed by the blue dashed box in (C) and the corresponding map of pseudo-magnetic fields derived from the strain tensors (bottom).

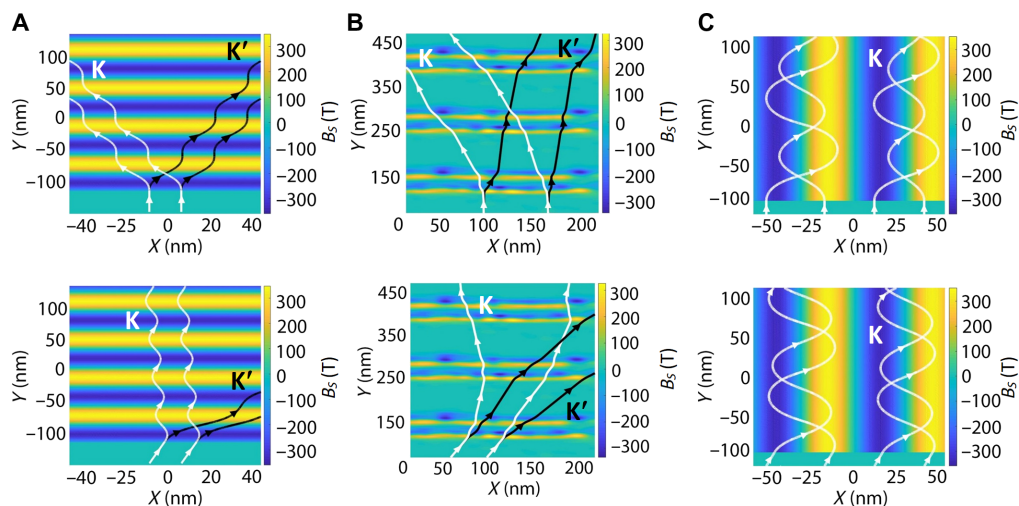


Fig. 5. Parallel graphene wrinkles as topological channels for valley splitting and valley-polarized propagation. (A) Simulations for parallel graphene wrinkles as a valley splitter, showing the trajectories of initially valley-degenerate ($K + K'$) fermions from strain-free regions becoming split when injected vertically into regions with strain-induced periodic channels of pseudo-magnetic fields. Top: Trajectories of K and K' fermions for an incident angle perpendicular to the parallel channels ($\theta = 0^\circ$). Bottom: Trajectories of K - and K' -valley fermions for an incident angle at $\theta = 15^\circ$ relative to the normal vector of the parallel channels. (B) Top: Simulated trajectories of K and K' fermions for an incident angle perpendicular to the realistic strain-induced parallel pseudo-magnetic fields ($\theta = 0^\circ$) shown in Fig. 4C. Bottom: Simulated trajectories of K and K' fermions for an incident angle at $\theta = 15^\circ$ relative to the normal vector of the realistic strain-induced parallel pseudo-magnetic fields shown in Fig. 4C. (C) Simulations for parallel graphene wrinkles as a valley propagator, showing the collimation of valley-polarized fermions. Top: Trajectories of K -valley fermions incident at an angle parallel to the channels ($\theta = 90^\circ$). Bottom: Trajectories of K -valley fermions incident at an angle $\theta = 75^\circ$ relative to the normal vector of the parallel channels.

associated with the two valleys (also known as two pseudo-spins) K and K' in reciprocal space are opposite in sign and give rise to a peculiar zero mode (36). This zero mode corresponds to a condensate where the Dirac fermions are delocalized over the entire sample, and yet they remain alternately localized and anti-localized for the pseudo-spin projection in the real space, yielding local spontaneous time-reversal symmetry breaking (36). Empirically, this spontaneous symmetry breaking may be manifested by the alternating presence and absence of the tunneling conductance peak at $n = 0$ for two inequivalent sublattices in graphene, which has been previously demonstrated by STS studies of molecular graphene (11). In this study, we also found that the point spectra of all strained regions exhibit statistically equal probabilities of the two zero modes. That is, the tunneling spectra at zero bias ($V = 0$) exhibit either a conductance peak or a conductance gap, as exemplified in fig. S8A for the zero-bias conductance map of strained graphene over a Pd tetrahedron and the corresponding histograms in fig. S8B. This finding therefore provides supporting evidence for spontaneous local time-reversal symmetry breaking due to strain-induced gauge potentials in real graphene.

Nanoscale strain engineering of graphene-based valleytronic/spintronic devices

The formation of periodic parallel graphene wrinkles by means of modern nanofabrication technology provides a pathway toward realizing controlled strain-induced effects for scalable development of graphene-based valleytronic devices. For instance, by patterning a valley Hall device configuration with the long-axis parallel to graphene wrinkles as schematically illustrated in fig. S9A, strong nonlocal resistance and VHEs may be detected under proper back-gated voltages, leading to a valley Hall transistor similar to previous observation of the VHE in exfoliated monolayer graphene-on-h-BN flakes (10). It

is also conceivable to obtain highly valley-polarized currents through the combination of valley splitters (Fig. 5, A and B) and valley propagators (Fig. 5C), as conceptually illustrated in fig. S9A. Furthermore, by injecting valley-polarized currents into strong spin-orbit coupled materials, the outgoing currents can become spin-polarized for spintronic applications (fig. S9B). Last, we note that many such devices can be developed by means of scalable and reproducible nanofabrication technology on large-area PECVD-grown graphene sheets (32), thus making the applications of graphene-based nanoscale valleytronic/spintronic devices closer to reality.

Strain-induced superconductivity in monolayer graphene

The discovery of superconductivity in bilayer graphene twisted at a “magic angle” (37) has kindled great interest in exploring “flat-band” materials (38) (i.e., materials with dispersionless energy versus momentum relation) for induction of superconductivity. A recent theoretical proposal (39) suggests that superconductivity may be more easily realized in topological flat bands induced by strain in graphene through periodic ripples and by including the effect of electronic correlation. It is argued that the chiral d -wave superconductivity may be stabilized under strain even for slightly doped graphene and that superconductivity thus derived could exhibit the long-sought-after superconducting states with nonvanishing center-of-mass momentum for Cooper pairs (39).

In the limit of $(J/t) \sim 1$ where J represents the antiferromagnetic coupling and t is the nearest-neighbor hopping energy, the theoretical conditions necessary for the occurrence of superconductivity are found to be $(h/L) \geq 0.05$ and $h^2/(La_0) \geq 1$, where h and L denote the height and periodic separation of the ripples, respectively, and $a_0 \approx 0.142$ nm is the nearest carbon-carbon distance for equilibrium graphene (39). For typical values of $h = 20$ nm and $L = 300$ nm in this work, we find $(h/L) \approx 0.067$ and $h^2/(La_0) \approx 9.39$ so that both

theoretical conditions are satisfied, implying possible occurrence of superconductivity if the premise of strong electronic correlation is justifiable (39). Given this intriguing prospect, it would be worthwhile to empirically explore possible strain-induced superconductivity in monolayer graphene with architected parallel wrinkles and to verify the validity of strong electronic correlation under giant pseudo-magnetic fields. However, empirical verifications of superconductivity require measurements at cryogenic temperatures. Given that the thermal expansion coefficient for graphene is negative and those for typical substrate materials (such as silicon) are positive, the strain induced by architected substrates in graphene is expected to decrease with decreasing temperature. Therefore, proper consideration of such complications will be necessary in the investigation of possible strain-induced superconductivity in graphene.

In summary, we have demonstrated a controlled approach to manipulating the topological states in monolayer graphene via nanoscale strain engineering. By placing strain-free monolayer graphene on architected nanostructures to induce global inversion symmetry breaking, we are able to induce giant pseudo-magnetic fields (up to ~ 800 T) with desirable spatial distributions, realize global valley polarization, and achieve periodic 1D topological channels for protected propagation of chiral fermion modes in strained graphene. The methodology presented in this work not only provides a platform for designing and controlling the gauge potential and Berry curvatures in graphene but also is promising for realizing scalable graphene-based valleytronic devices and strain-induced superconductivity.

MATERIALS AND METHODS

Graphene/BN/Pd tetrahedron sample preparation

In this work, the Pd tetrahedron NCs were synthesized by a wet-chemical method (33). The preparation procedure is briefly summarized below. We mixed 7.6 mg of palladium (II) acetylacetonate $[\text{Pd}(\text{acac})_2]$, 16.5 mg of iron (II) acetylacetonate $[\text{Fe}(\text{acac})_2]$, 50.0 mg of polyvinylpyrrolidone, and 10.0 ml of *N,N'*-dimethylformamide into a 30-ml vial. After ultrasonication for 5 min, the mixture was heated at 120°C for 10 hours in an oil bath on a hotplate. The resulting precipitant were collected by centrifugation and rinsed with ethanol several times. A Si substrate was first ultrasonicated in acetone and subsequently in isopropyl alcohol for 10 min each, blown dry with dry nitrogen, and then loaded into a 100-W O_2 plasma for 5 min to remove any traces of hydrocarbon residue. The Pd tetrahedron suspension was dropped onto the Si substrate and spun at 1500 RPM for 1 min. After the spin-coating process, the sample was loaded into a 100-W O_2 plasma for 5 min again to remove any residue on the Pd tetrahedron NCs. The resulting typical size of the Pd tetrahedron NCs ranges from 50 to 70 nm and the height ranges from 40 to 60 nm, as exemplified in Fig. 1 (B and C). Next, a monolayer BN was transferred over the substrate covered by the Pd tetrahedron NCs, followed by the transfer of PECVD-graphene onto the BN/Pd-NCs. AFM and SEM measurements were performed on every step of the process. We found that graphene/BN conformed very well to the Pd tetrahedron NCs if they were well separated from each other, as exemplified by the AFM image in Fig. 1 (D and E, top). However, we found that graphene tended to form wrinkles along the Pd tetrahedrons if they were sufficiently closed to each other, as exemplified by the AFM images in the bottom panel of Fig. 1E. This situation is similar to our previous observation of graphene/h-BN on Au nanoparticles and graphene/h-BN on Si nanostructures (31).

Procedures for fabricating periodic arrays of graphene/h-BN/SiO₂ nano-cones

SiO₂ nano-cone substrate fabrication is schematically shown in fig. S4 and further described here. First, a typical e-beam lithography method was used to pattern an array of discs with ~ 50 nm diameters on a Si substrate with a 300-nm oxide layer. After development, 15-nm-thick Ni is deposited and used as a mask in a $\text{C}_4\text{F}_8/\text{O}_2$ reactive ion etching environment to create Si nano-pillars. After etching, the substrate was immersed in the buffered oxide etch for ~ 20 s until the Ni discs fell from the top of the nano-cones. A typical size of nano-cone is ~ 40 nm in diameter and ~ 20 nm in height. A monolayer h-BN was transferred over the SiO₂ nano-cones, followed by the transfer of PECVD-grown graphene.

Scanning tunneling microscopic and spectroscopic studies of strain-engineered graphene

Two types of monolayer strained graphene samples were investigated using STM/STS at room temperature. The samples were loaded onto our homemade STM system and pumped down to a vacuum level of 1.6×10^{-6} torr. Atomically resolved topographic and spectroscopic measurements were carried out on samples at room temperature using a Pt/Ir STM tip with a typical tunnel junction resistance at 2 gigaohms.

SUPPLEMENTARY MATERIALS

Supplementary materials for this article is available at <http://advances.sciencemag.org/cgi/content/full/6/19/eaat9488/DC1>

REFERENCES AND NOTES

- M. V. Berry, Quantal phase factors accompanying adiabatic changes. *Proc. R. Soc. London* **A392**, 45–57 (1984).
- G. P. Mikitik, Y. V. Sharlai, Manifestation of Berry's phase in metal physics. *Phys. Rev. Lett.* **82**, 2147–2250 (1999).
- D. Xiao, M.-C. Chang, Q. Niu, Berry phase effects on electronic properties. *Rev. Mod. Phys.* **82**, 1959–2007 (2010).
- D. J. Thouless, M. Kohmoto, M. P. Nightingale, M. den Nijs, Quantized Hall conductance in a two-dimensional periodic potential. *Phys. Rev. Lett.* **49**, 405 (1982).
- X.-L. Qi, S.-C. Zhang, The quantum spin Hall effect and topological insulators. *Phys. Today* **63**, 33–38 (2010).
- M. Z. Hasan, C. L. Kane, *Colloquium: Topological insulators*. *Rev. Mod. Phys.* **82**, 3045–3067 (2010).
- A. H. Castro Neto, F. Guinea, N. M. R. Peres, K. S. Novoselov, A. K. Geim, The electronic properties of graphene. *Rev. Mod. Phys.* **81**, 109–162 (2009).
- F. Zhang, A. H. MacDonald, E. J. Mele, Valley Chern numbers and boundary modes in gapped bilayer graphene. *Proc. Natl. Acad. Sci. U.S.A.* **110**, 10546–10551 (2013).
- Y. Zhang, Y.-W. Tan, H. L. Stormer, P. Kim, Experimental observation of the quantum Hall effect and Berry's phase in graphene. *Nature* **438**, 201–204 (2005).
- R. V. Gorbachev, J. C. W. Song, G. L. Yu, A. V. Kretinin, F. Withers, Y. Cao, A. Mishchenko, I. V. Grigorieva, K. S. Novoselov, L. S. Levitov, A. K. Geim, Detecting topological currents in graphene superlattices. *Science* **346**, 448–451 (2014).
- K. K. Gomes, W. Mar, W. Ko, F. Guinea, H. C. Manoharan, Designer Dirac fermions and topological phases in molecular graphene. *Nature* **483**, 306–310 (2012).
- L. Ju, Z. Shi, N. Nair, Y. Lv, C. Jin, J. Velasco Jr., C. Ojeda-Aristizabal, H. A. Bechtel, M. C. Martin, A. Zettl, J. Analytis, F. Wang, Topological valley transport at bilayer graphene domain walls. *Nature* **520**, 650–655 (2015).
- D. Xiao, G.-B. Liu, W. Feng, X. Xu, W. Yao, Coupled spin and valley physics in monolayers of MoS₂ and other group-VI dichalcogenides. *Phys. Rev. Lett.* **108**, 196802 (2012).
- K. F. Mak, K. He, J. Shan, T. F. Heinz, Control of valley polarization in monolayer MoS₂ by optical helicity. *Nat. Nanotechnol.* **7**, 494–498 (2012).
- K. S. Novoselov, A. Mishchenko, A. Carvalho, A. H. C. Neto, 2D materials and van der Waals heterostructures. *Science* **353**, 6298 (2016).
- S. Manzeli, D. Ovchinnikov, D. Pasquier, O. V. Yazyev, A. Kis, 2D transition metal dichalcogenides. *Nat. Rev. Mater.* **2**, 17033 (2017).
- A. J. Pearce, E. Mariani, G. Burkard, Tight-binding approach to strain and curvature in monolayer transition-metal dichalcogenides. *Phys. Rev. B* **94**, 155416 (2016).

18. H. Li, A. W. Contryman, X. Qian, S. M. Ardakani, Y. Gong, X. Wang, J. M. Weisse, C. H. Lee, J. Zhao, P. M. Ajayan, J. Li, H. C. Manoharan, X. Zheng, Optoelectronic crystal of artificial atoms in strain-textured molybdenum disulphide. *Nat. Commun.* **6**, 7381 (2015).
19. A. Reserbat-Plantey, D. Kalita, Z. Han, L. Ferlazzo, S. Autier-Laurent, K. Komatsu, C. Li, R. Weil, A. Ralko, L. Marty, S. Guéron, N. Bendiab, H. Bouchiat, V. Bouchiat, Strain superlattices and macroscale suspension of graphene induced by corrugated substrates. *Nano Lett.* **14**, 5044–5051 (2014).
20. H. Tomori, A. Kanda, H. Goto, Y. Ootuka, K. Tsukagoshi, S. Moriyama, E. Watanabe, D. Tsuya, Introducing nonuniform strain to graphene using dielectric nanopillars. *Appl. Phys. Express* **4**, 075102 (2011).
21. J. Choi, H. J. Kim, M. C. Wang, J. Leem, W. P. King, S. W. Nam, Three-dimensional integration of graphene via swelling, shrinking, and adaptation. *Nano Lett.* **15**, 4525–4531 (2015).
22. B. Pacakova, T. Verhagen, M. Bousa, U. Hübner, J. Vejpravova, M. Kalbac, O. Frank, Mastering the wrinkling of self-supported graphene. *Sci. Rep.* **7**, 10003 (2017).
23. Y. Zhang, M. Heiraniyan, B. Janicek, Z. Budrikis, S. Zapperi, P. Y. Huang, H. T. Johnson, N. R. Aluru, J. W. Lyding, N. Mason, Strain modulation of graphene by nanoscale substrate curvatures: A molecular view. *Nano Lett.* **18**, 2098–2104 (2018).
24. Y. Jiang, J. Mao, J. Duan, X. Lai, K. Watanabe, T. Taniguchi, E. Y. Andrei, Visualizing strain-induced pseudomagnetic fields in graphene through an hBN magnifying glass. *Nano Lett.* **17**, 2839–2843 (2017).
25. J. L. Mañes, Symmetry-based approach to electron-phonon interactions in graphene. *Phys. Rev. B* **76**, 045430 (2007).
26. F. Guinea, M. I. Katsnelson, M. A. H. Vozmediano, Midgap states and charge inhomogeneities in corrugated graphene. *Phys. Rev. B* **77**, 075422 (2008).
27. F. Guinea, M. I. Katsnelson, A. K. Geim, Energy gaps and a zero-field quantum Hall effect in graphene by strain engineering. *Nat. Phys.* **6**, 30–33 (2010).
28. M. L. Teague, A. P. Lai, J. Velasco, C. R. Hughes, A. D. Beyer, M. W. Bockrath, C. N. Lau, N.-C. Yeh, Evidence for strain-induced local conductance modulations in single-layer graphene on SiO₂. *Nano Lett.* **9**, 2542–2546 (2009).
29. N. Levy, S. A. Burke, K. L. Meaker, M. Panlasigui, A. Zettl, F. Guinea, A. H. C. Neto, M. F. Crommie, Strain-induced Pseudo-Magnetic fields greater than 300 Tesla in graphene nanobubbles. *Science* **329**, 544–547 (2010).
30. N.-C. Yeh, M.-L. Teague, S. Yeom, B. L. Standley, R. T.-P. Wu, D. A. Boyd, M. W. Bockrath, Strain-induced pseudo-magnetic fields and charging effects on CVD-grown graphene. *Surf. Sci.* **605**, 1649–1656 (2011).
31. N.-C. Yeh, C.-C. Hsu, M. L. Teague, J.-Q. Wang, D. A. Boyd, C.-C. Chen, Nanoscale strain engineering of graphene and graphene-based devices. *Acta Mech. Sin.* **32**, 497–509 (2016).
32. D. A. Boyd, W.-H. Lin, C.-C. Hsu, M. L. Teague, C.-C. Chen, Y.-Y. Lo, W.-Y. Chan, W.-B. Su, T.-C. Cheng, C.-S. Chang, C.-I. Wu, N.-C. Yeh, Single-step deposition of high-mobility graphene at reduced temperatures. *Nat. Commun.* **6**, 6620 (2015).
33. Y. Zhang, M. Wang, E. Zhu, Y. Zheng, Y. Huang, X. Huang, Seedless growth of palladium nanocrystals with tunable structures: From tetrahedra to nanosheets. *Nano Lett.* **15**, 7519–7525 (2015).
34. W.-H. Lin, T.-H. Chen, J.-K. Chang, J.-I. Taur, Y.-Y. Lo, W.-L. Lee, C.-S. Chang, W.-B. Su, C.-I. Wu, A direct and polymer-free method for transferring graphene grown by chemical vapor deposition to any substrate. *ACS Nano* **8**, 1784–1791 (2014).
35. W.-H. Lin, V. W. Brar, D. Jariwala, M. C. Sherrott, W.-S. Tseng, C.-I. Wu, N.-C. Yeh, H. A. Atwater, Atomic-scale structural and chemical characterization of hexagonal boron nitride layers synthesized at the wafer-scale with monolayer thickness control. *Chem. Mater.* **29**, 4700–4707 (2017).
36. I. F. Herbut, Pseudomagnetic catalysis of the time-reversal symmetry breaking in graphene. *Phys. Rev. B* **78**, 205433 (2008).
37. Y. Cao, V. Fatemi, A. Demir, S. Fang, S. L. Tomarken, J. Y. Luo, J. D. Sanchez-Yamagishi, K. Watanabe, T. Taniguchi, E. Kaxiras, R. C. Ashoori, P. Jarillo-Herrero, Correlated insulator behaviour at half-filling in magic-angle graphene superlattices. *Nature* **556**, 80–84 (2018).
38. R. Bistritzer, A. H. MacDonald, Moiré bands in twisted double-layer graphene. *Proc. Natl. Acad. Sci. U.S.A.* **108**, 12233–12237 (2011).
39. F. Xu, P.-H. Chou, C.-H. Chung, T.-K. Lee, C.-Y. Mou, Strain-induced superconducting pair density wave states in graphene. *Phys. Rev. B* **98**, 205103 (2018).
40. M. Neek-Amal, F. M. Peeters, Graphene on boron-nitride: Moiré pattern in the van der Waals energy. *Appl. Phys. Lett.* **104**, 041909 (2014).

Acknowledgments

Funding: The authors gratefully acknowledge joint support for this work by the Army Research Office under the MURI program (award #W911NF-16-1-0472), the National Science Foundation under the Physics Frontier Centers program for the Institute for Quantum Information and Matter (IQIM) at the California Institute of Technology (award #1733907), and the Kavli Foundation. **Author contributions:** N.-C.Y. conceived the ideas and coordinated the research project. C.-C.H. synthesized and characterized the strain-free monolayer graphene, developed architected nanostructures, transferred monolayer graphene and monolayer h-BN to the architected nanostructures for strain engineering, and carried out the SEM and AFM studies. M.L.T. performed the STM/STS studies on strained graphene and analyzed the topographic and spectroscopic data. J.-Q.W. carried out the MD simulations to map out the strain-induced pseudo-magnetic fields and developed a semi-classical model to determine the trajectories of valley-polarized Dirac fermions. N.-C.Y. wrote the paper with contributions from all coauthors. **Competing interests:** The authors declare that they have no competing interests. **Data and materials availability:** All data needed to evaluate the conclusions in the paper are present in the paper and/or the Supplementary Materials. Additional data related to this paper may be requested from the authors.

Submitted 29 April 2019

Accepted 14 February 2020

Published 8 May 2020

10.1126/sciadv.aat9488

Citation: C.-C. Hsu, M. L. Teague, J.-Q. Wang, N.-C. Yeh, Nanoscale strain engineering of giant pseudo-magnetic fields, valley polarization, and topological channels in graphene. *Sci. Adv.* **6**, eaat9488 (2020).

Nanoscale strain engineering of giant pseudo-magnetic fields, valley polarization, and topological channels in graphene

C.-C. Hsu, M. L. Teague, J.-Q. Wang and N.-C. Yeh

Sci Adv 6 (19), eaat9488.
DOI: 10.1126/sciadv.aat9488

ARTICLE TOOLS	http://advances.sciencemag.org/content/6/19/eaat9488
SUPPLEMENTARY MATERIALS	http://advances.sciencemag.org/content/suppl/2020/05/04/6.19.eaat9488.DC1
REFERENCES	This article cites 40 articles, 4 of which you can access for free http://advances.sciencemag.org/content/6/19/eaat9488#BIBL
PERMISSIONS	http://www.sciencemag.org/help/reprints-and-permissions

Use of this article is subject to the [Terms of Service](#)

Science Advances (ISSN 2375-2548) is published by the American Association for the Advancement of Science, 1200 New York Avenue NW, Washington, DC 20005. The title *Science Advances* is a registered trademark of AAAS.

Copyright © 2020 The Authors, some rights reserved; exclusive licensee American Association for the Advancement of Science. No claim to original U.S. Government Works. Distributed under a Creative Commons Attribution NonCommercial License 4.0 (CC BY-NC).